inorganics

MDPI

Article

Improved Oxide Ion Conductivity of Hexagonal Perovskite-Related Oxides $Ba_3W_{1+x}V_{1-x}O_{8.5+x/2}$

Yugo Kikuchi [1,†], Yuta Yasui [1,†], James R. Hester [2] and Masatomo Yashima [1,*,†]

[1] Department of Chemistry, School of Science, Tokyo Institute of Technology, 2-12-1 W4–17 O-okayama, Meguro-ku, Tokyo 152-8551, Japan
[2] Australian Centre for Neutron Scattering, Australian Nuclear Science and Technology Organisation (ANSTO), Locked Bag 2001, Kirrawee DC, Sydney, NSW 2232, Australia
* Correspondence: yashima@cms.titech.ac.jp
† These authors contributed equally to this work.

Abstract: Hexagonal perovskite-related oxides such as $Ba_3WVO_{8.5}$ have attracted much attention due to their unique crystal structures and significant oxide ion conduction. However, the oxide ion conductivity of $Ba_3WVO_{8.5}$ is not very high. Herein, we report new hexagonal perovskite-related oxides $Ba_3W_{1+x}V_{1-x}O_{8.5+x/2}$ ($x = -0.1, -0.05, 0.05, 0.1, 0.25, 0.4, 0.5, 0.6$, and 0.75). The bulk conductivity of $Ba_3W_{1.6}V_{0.4}O_{8.8}$ was found to be 21 times higher than that of the mother material $Ba_3WVO_{8.5}$ at 500 °C. Maximum entropy method (MEM) neutron scattering length density (NSLD) analyses of neutron diffraction data at 800 °C experimentally visualized the oxide ion diffusion pathways through the octahedral O2 and tetrahedral O3 sites in intrinsically oxygen-deficient layers. By increasing the excess W content x in $Ba_3W_{1+x}V_{1-x}O_{8.5+x/2}$, the excess oxygen content $x/2$ increases, which leads to more oxygen atoms at the O2 and O3 oxygen sites, a higher minimum NSLD on the O2–O3 path, and a higher level of conductivity. Another reason for the increased conductivity of $Ba_3W_{1.6}V_{0.4}O_{8.8}$ is the lower activation energy for oxide ion conduction, which can be ascribed to the longer (W/V)–O2 and (W/V)–O3 distances due to the substitution of V atoms with large-sized W species. The present findings open new avenues in the science and technology of oxide ion conductors.

Keywords: oxide ion conductivity; hexagonal perovskite; crystal structure; neutron diffraction; solid oxide fuel cells; Rietveld analysis; new material; electrical conductivity; band gap; maximum entropy method

check for updates

Citation: Kikuchi, Y.; Yasui, Y.; Hester, J.R.; Yashima, M. Improved Oxide Ion Conductivity of Hexagonal Perovskite-Related Oxides $Ba_3W_{1+x}V_{1-x}O_{8.5+x/2}$. *Inorganics* **2023**, *11*, 238. https://doi.org/10.3390/inorganics11060238

Academic Editor: Nataliia Tarasova

Received: 8 May 2023
Revised: 25 May 2023
Accepted: 26 May 2023
Published: 29 May 2023

1. Introduction

Oxide ion and proton conductors are important materials for clean energy and environment [1–14]. For example, oxide ion conductors can be used in electrochemical devices such as solid oxide fuel cells (SOFCs) and solid oxide electrolyzer cells (SOECs). High oxide ion conductivity is needed for high-performance electrochemical devices and is attained in materials with specific crystal structures such as the fluorite-type and AMO_3 perovskite-type structures [10,11,15–17]. Here, A and M are relatively larger and smaller cations. The conventional yttria-stabilized zirconia (YSZ) electrolytes exhibit low levels of oxide ion conductivity at intermediate temperatures, which restrict the widespread use of SOFCs with YSZ electrolytes. To solve this problem, it is of vital importance to search for new oxide ion conductors that exhibit higher conductivities.

There are four main groups of perovskite-type and perovskite-related structures: (i) the AMO_3-perovskite-type structure, (ii) AMO_3-perovskite-related structure, (iii) hexagonal perovskite-related structure, and (iv) modular structure [18,19]. Layered perovskites are emerging materials with layered structures that have perovskite or perovskite-like units [11]. The hexagonal perovskite-related oxides (iii) have a layered structure containing a hexagonal close-packed AO_3 h layer or an oxygen-deficient, hexagonal close-packed $AO_{3-\delta}$

h′ layer [9,11,12,18–27]. Compared with other perovskites, high levels of oxide ion and proton conduction were rarely found in hexagonal perovskite-related materials. Recently, high oxide ion conduction has been reported in various hexagonal perovskite-related oxides such as $Ba_3MoNbO_{8.5}$, $Ba_3WVO_{8.5}$, and $Ba_7Nb_{3.9}Mo_{1.1}O_{20.05}$ [18,20,21,24–27]. $Ba_3M_2O_{8.5}$ oxides (e.g., M_2 = MoNb, WV, and WNb) exhibit structural disorder in the oxygen-deficient, cubic close-packed c′ layer, leading to significant oxide ion conduction [19–22,24–27]. A high level of occupational disorder at the octahedral O2 and tetrahedral O3 sites yields a high probability density of oxygen atoms between the O2 and O3 sites, leading to a high level of oxide ion conductivity [27]. A possible means of increasing the probability density of oxygen atoms on the O2–O3 pathway is to have a larger amount of excess oxygen. Thus, the oxide ion conductivity of $Ba_3WVO_{8.5}$ can be expected to increase by increasing the amount of oxygen $8.5+x/2$ via W/V substitution in $Ba_3W_{1+x}V_{1-x}O_{8.5+x/2}$. Herein, we report new hexagonal perovskite-related oxides $Ba_3W_{1+x}V_{1-x}O_{8.5+x/2}$ and their improved oxide ion conductivity compared with the mother material, $Ba_3WVO_{8.5}$. In the present work, we demonstrate that the bulk conductivity of $Ba_3W_{1.6}V_{0.4}O_{8.8}$ is 21 times higher than that of mother material $Ba_3WVO_{8.5}$ at 500 °C, which is ascribed to the greater amount of excess oxygen atoms $O_{0.3}$ and the lower activation energy for oxide ion conduction in $Ba_3W_{1.6}V_{0.4}O_{8.8}$.

2. Results and Discussion

2.1. Formation of $Ba_3W_{1+x}V_{1-x}O_{8.5+x/2}$ Solid Solutions and Their Electrical Conductivities

$Ba_3W_{1+x}V_{1-x}O_{8.5+x/2}$ (x = −0.1, −0.05, 0, 0.05, 0.1, 0.25, 0.4, 0.5, 0.6, and 0.75) oxides were prepared via solid-state reactions. Most of their X-ray powder diffraction (XRD) peaks at room temperature (RT) were indexed to a rhombohedral lattice, indicating that the main phase of $Ba_3W_{1+x}V_{1-x}O_{8.5+x/2}$ is rhombohedral (space group: *R*3*m* and crystal symmetry: trigonal), which is consistent with the phase identification of $Ba_3WVO_{8.5}$ in the literature [21,22]. Figure S1a is a typical XRD pattern of $Ba_3W_{1.6}V_{0.4}O_{8.8}$, showing the main rhombohedral phase in addition to a small amount of $BaWO_4$ phase. The lattice volume and lattice parameter c of $Ba_3W_{1+x}V_{1-x}O_{8.5+x/2}$ decrease with increasing excess W content x in the compositional range from x = 0.1 to 0.6, (Figure S1b,c), suggesting the formation of rhombohedral $Ba_3W_{1+x}V_{1-x}O_{8.5+x/2}$ solid solutions.

Figure 1a shows the Arrhenius plots of the direct current (DC) electrical conductivity σ_{DC} of $Ba_3W_{1+x}V_{1-x}O_{8.5+x/2}$ (x = −0.1, −0.05, 0, 0.05, 0.1, 0.25, 0.4, 0.5, 0.6, and 0.75) in static air. The σ_{DC} increases with increasing temperature. At any temperature between 600 and 1000 °C, the corrected full-density DC electrical conductivity $\sigma_{DC/corr}$ increases with an increase in excess W content x in $Ba_3W_{1+x}V_{1-x}O_{8.5+x/2}$ from x = −0.1 to 0.6, which can be ascribed to the increase in carrier concentration due to the increase in excess oxygen atoms $x/2$ in $Ba_3W_{1+x}V_{1-x}O_{8.5+x/2}$ (Figure 1b). Meanwhile the $\sigma_{DC/corr}$ for x = 0.75 is lower than that for x = 0.6, over the entire temperature range, which can be ascribed to overdoping due to defect association and/or a greater amount of $BaWO_4$ impurity in the x = 0.75 sample. Similar overdoping has been observed in other hexagonal perovskite-related oxides, such as $Ba_7Ta_{4-x}Mo_{1+x}O_{20+x/2}$ [26]. $Ba_3W_{1.6}V_{0.4}O_{8.8}$ exhibits the highest conductivity σ_{DC} among $Ba_3W_{1+x}V_{1-x}O_{8.5+x/2}$ (x = −0.1, −0.05, 0, 0.05, 0.1, 0.25, 0.4, 0.5, 0.6, and 0.75) over the entire temperature range (Figure 1a,b). Therefore, we focus on $Ba_3W_{1.6}V_{0.4}O_{8.8}$ for further studies. For example, at 600 °C, the σ_{DC} of $Ba_3W_{1.6}V_{0.4}O_{8.8}$ (3.0×10^{-4} S cm^{-1}) is 86 times higher than that of the mother material, $Ba_3WVO_{8.5}$ (3.5×10^{-6} S cm^{-1}). The σ_{DC} values of $Ba_3W_{1.6}V_{0.4}O_{8.8}$ at 800 and 1000 °C were as high as 3.7×10^{-3} and 0.021 S cm^{-1}, respectively.

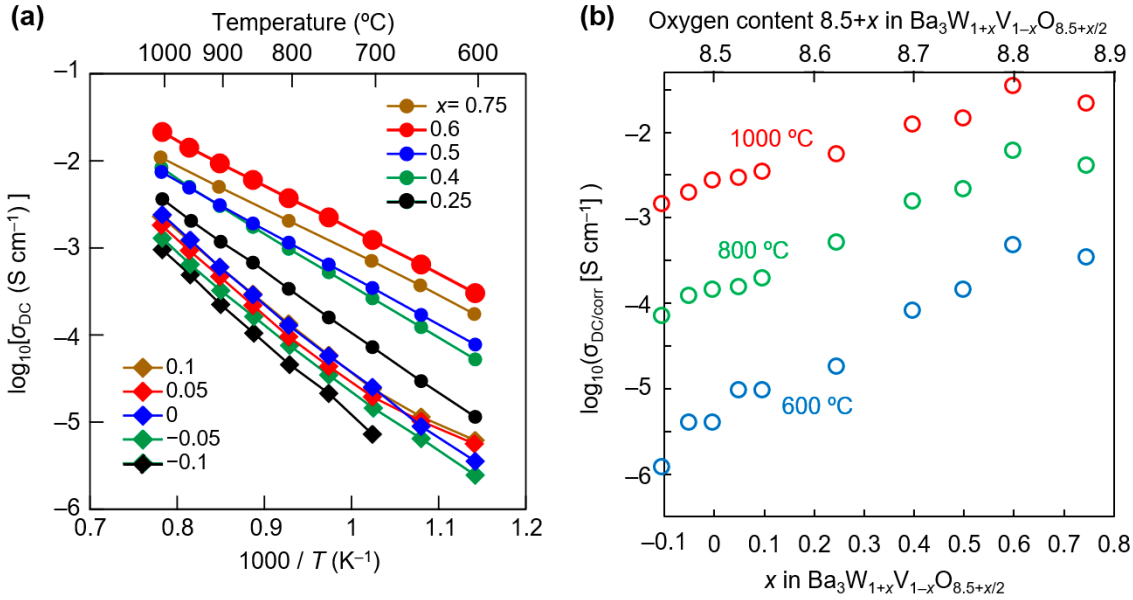

Figure 1. (**a**) Arrhenius plots of DC electrical conductivities σ_{DC} of $Ba_3W_{1+x}V_{1-x}O_{8.5+x/2}$ (x = −0.1, −0.05, 0, 0.05, 0.1, 0.25, 0.4, 0.5, 0.6, and 0.75) in static air. (**b**) Variation of the corrected full-density DC electrical conductivity $\sigma_{DC/corr}$ at constant temperature in static air with the excess W content x (oxygen content = 8.5 + $x/2$) in $Ba_3W_{1+x}V_{1-x}O_{8.5+x/2}$. $\sigma_{DC/corr} = 2\sigma_{DC}/(2 - 3p)$, where the p is porosity [28].

2.2. Oxide Ion Conduction of $Ba_3W_{1.6}V_{0.4}O_{8.8}$

X-ray photoelectron spectroscopy (XPS) spectra of $Ba_3W_{1.6}V_{0.4}O_{8.8}$ and $Ba_3WVO_{8.5}$ showed that the valences of W and V at RT were +6 and +5, respectively, (Figure S2), indicating $(Ba^{2+})_3(W^{6+})_{1.6}(V^{5+})_{0.4}(O^{2-})_{8.8}$ and $(Ba^{2+})_3(W^{6+})(V^{5+})(O^{2-})_{8.5}$. The thermogravimetric analyses in dry air indicated no significant weight change in the second and third heating/cooling cycles (Figure S3), demonstrating no change in oxygen content. Therefore, the chemical compositions at a high temperature of 800 °C are the same as those at RT.

Figure 2a shows the oxygen partial pressure $P(O_2)$ dependence of the DC electrical conductivity σ_{DC} of $Ba_3W_{1.6}V_{0.4}O_{8.8}$ at 820 °C in dry conditions. The σ_{DC} increases with a decrease in $P(O_2)$ below 10^{-18} atm, suggesting electronic conduction due to the reduction in W and/or V cations. Meanwhile the σ_{DC} is almost independent of $P(O_2)$ between 10^{-17} and 0.21 atm at 820 °C, indicating that the influence of the p-type conducting $BaWO_4$ impurity on the σ_{DC} is negligible (See the Supplementary Note in the Supporting Information). The UV-vis reflectance spectra of $Ba_3W_{1.6}V_{0.4}O_{8.8}$ indicated a wide optical band gap (Figure S4), suggesting an electronic insulator. To examine possible proton conduction, the σ_{DC} was also measured in wet and dry air. The σ_{DC} values in wet air almost agree with those in dry air (Figure 2b). These results suggest oxide ion conduction in $Ba_3W_{1.6}V_{0.4}O_{8.8}$.

Impedance measurements of $Ba_3W_{1.6}V_{0.4}O_{8.8}$ were carried out in dry air to obtain its bulk conductivity. The impedance data were analyzed using the equivalent circuits shown in Figure S5 to extract the bulk and grain boundary conductivities. Figure 2c shows typical Nyquist plots of $Ba_3W_{1.6}V_{0.4}O_{8.8}$, with the bulk and grain boundary components indicated by semicircles. The bulk conductivity in dry air σ_b of $Ba_3W_{1.6}V_{0.4}O_{8.8}$ increases with increasing temperature and is as high as 3.0×10^{-3} S cm^{-1} at 794 °C. The activation energy for σ_b is lower than the activation energy for grain boundary conductivity (Figure S6). The σ_b of $Ba_3W_{1.6}V_{0.4}O_{8.8}$ is higher than that of the mother material $Ba_3WVO_{8.5}$ (e.g., it is 21 times higher at 500 °C). The σ_b of $Ba_3W_{1.6}V_{0.4}O_{8.8}$ is higher than that of $Ba_3WNbO_{8.5}$ below 500 °C [20] and is comparable to that of $Ba_3MoNbO_{8.5}$ around 370 °C [24], indicating that $Ba_3W_{1.6}V_{0.4}O_{8.8}$ is a superior oxide ion conductor. The higher σ_b of $Ba_3W_{1.6}V_{0.4}O_{8.8}$ compared to $Ba_3WVO_{8.5}$ is attributable to both the lower activation energy for σ_b and the higher carrier concentration (a larger oxygen content of 8.8) of

$Ba_3W_{1.6}V_{0.4}O_{8.8}$ compared to $Ba_3WVO_{8.5}$. The structural origins of the lower activation energy and higher carrier concentration will be described below.

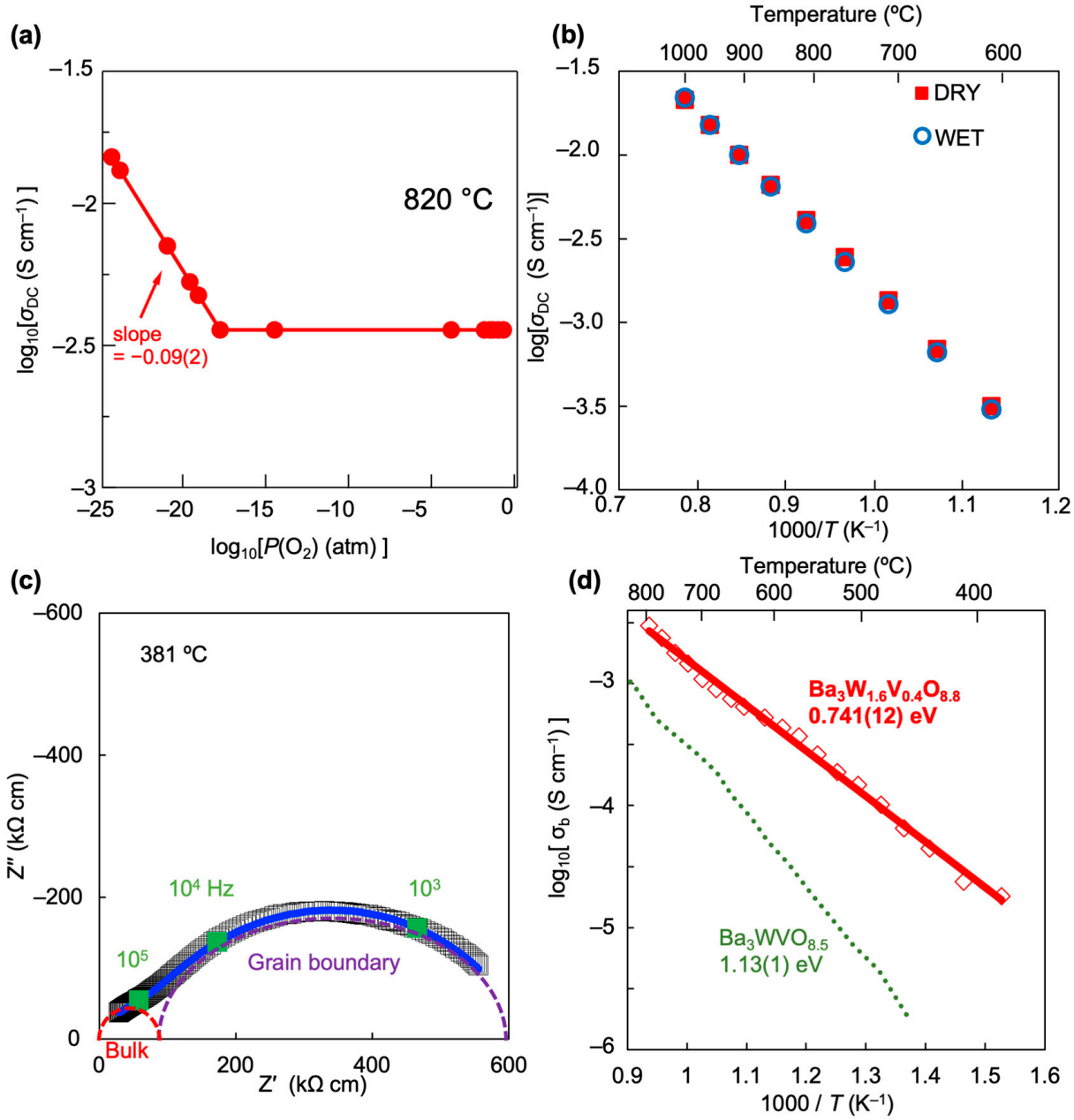

Figure 2. Oxide ion conduction of $Ba_3W_{1.6}V_{0.4}O_{8.8}$. (**a**) Oxygen partial pressure $P(O_2)$ dependence of the DC electrical conductivity σ_{DC} of $Ba_3W_{1.6}V_{0.4}O_{8.8}$ at 820 °C in dry conditions. (**b**) Arrhenius plots of σ_{DC} in wet and dry air. (**c**) Complex impedance plots of $Ba_3W_{1.6}V_{0.4}O_{8.8}$ in dry air at 381 °C. (**d**) Arrhenius plots of the bulk conductivity σ_b of $Ba_3W_{1.6}V_{0.4}O_{8.8}$ (red open diamonds and line) and $Ba_3WVO_{8.5}$ (light green dotted line [21]) in dry air.

2.3. Crystal Structure Analyses of $Ba_3W_{1.6}V_{0.4}O_{8.8}$ and $Ba_3WVO_{8.5}$

To investigate the origin of its high oxide ion conductivity, the crystal structure was analyzed using neutron diffraction data of $Ba_3W_{1.6}V_{0.4}O_{8.8}$ and $Ba_3WVO_{8.5}$ taken in situ at 18 and 800 °C (Figure 3). Rietveld analyses of $Ba_3W_{1.6}V_{0.4}O_{8.8}$ and $Ba_3WVO_{8.5}$ were successfully carried out as a hybrid structure (space group: *R*3*m*, Figure 4). Figure 3 shows the Rietveld patterns, indicating satisfactory fits. Preliminary structure analyses indicated no significant occupancy of W/V atoms at the Wyckoff position 3*b* and full

occupancy of W/V atoms at the 6*c* position (W/V site), indicating the chemical order of W/V atoms and W/V vacancies. Anisotropic atomic displacement parameters (ADPs) provided lower reliability factors than isotropic ADPs for Ba1, Ba2, O1, and O2 atoms. A split-atom model for the apical oxygen O3 at the 36*i* Wyckoff position yielded lower reliability factors compared with a non-split atom model. Therefore, we used anisotropic ADPs for Ba1, Ba2, O1, and O2 atoms and a split-atom model for the O3 atom in the final refinements. The refined crystal parameters and reliability factors are listed in Tables S1–S4. The bond valence sums of the Ba1, Ba2, W, V, and O1 atoms agree with their valences of +2, +2, +6, +5, and −2, validating the refined crystal structures. The crystal parameters of $Ba_3WVO_{8.5}$ at room temperature and at 800 °C obtained in this work are consistent with those reported in the literature [21,22].

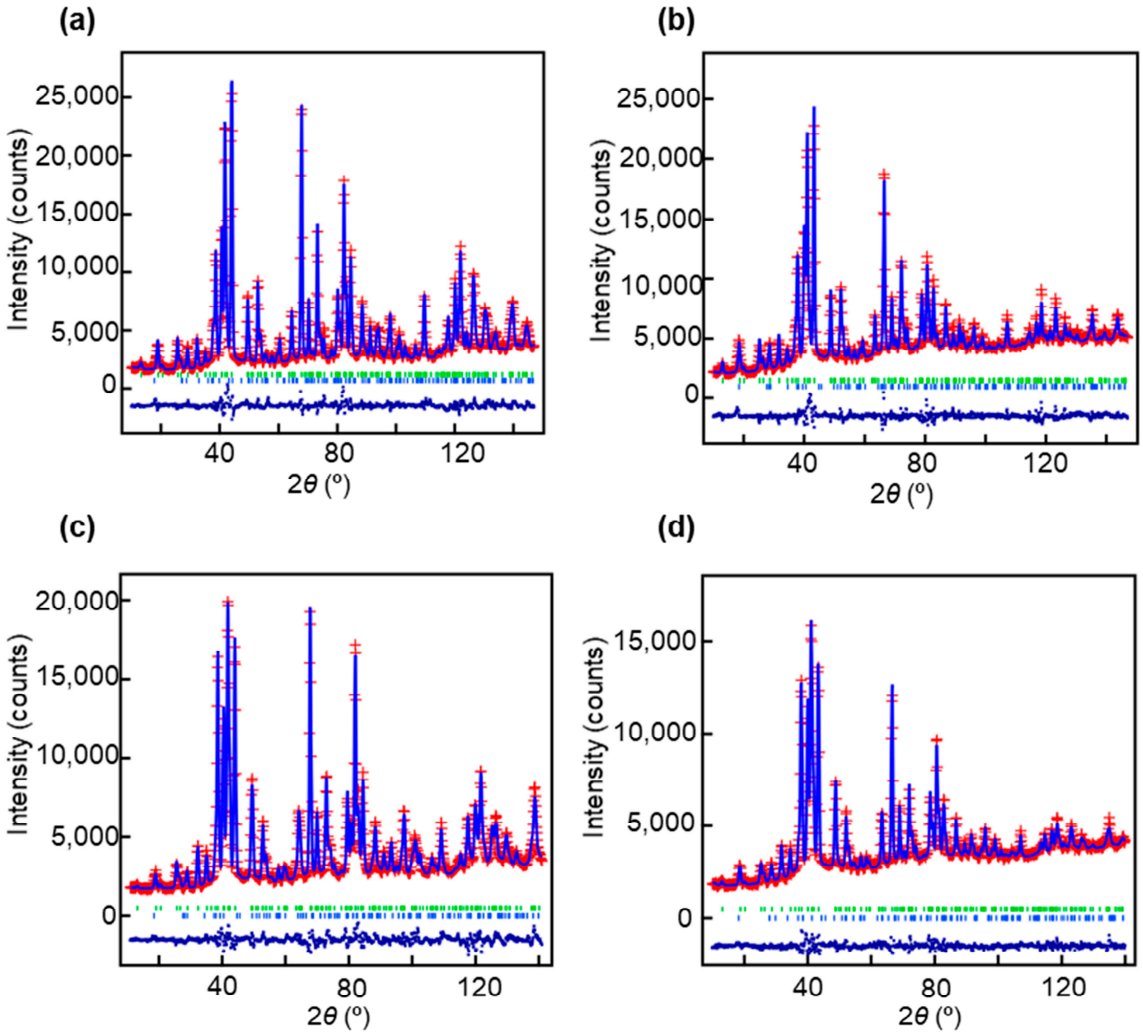

Figure 3. Rietveld patterns of neutron diffraction data of $Ba_3W_{1.6}V_{0.4}O_{8.8}$ measured at (**a**) 18 °C and (**b**) 800 °C. Rietveld patterns of neutron diffraction data of $Ba_3WVO_{8.5}$ at (**c**) 18 °C and (**d**) 800 °C. Red crosses and blue lines denote the observed and calculated intensities, respectively, and blue dots below show the difference patterns. Green and blue tick marks stand for the calculated peak positions of the rhombohedral *R*3*m* $Ba_3W_{1.6}V_{0.4}O_{8.8}$ phase and $BaWO_4$, respectively.

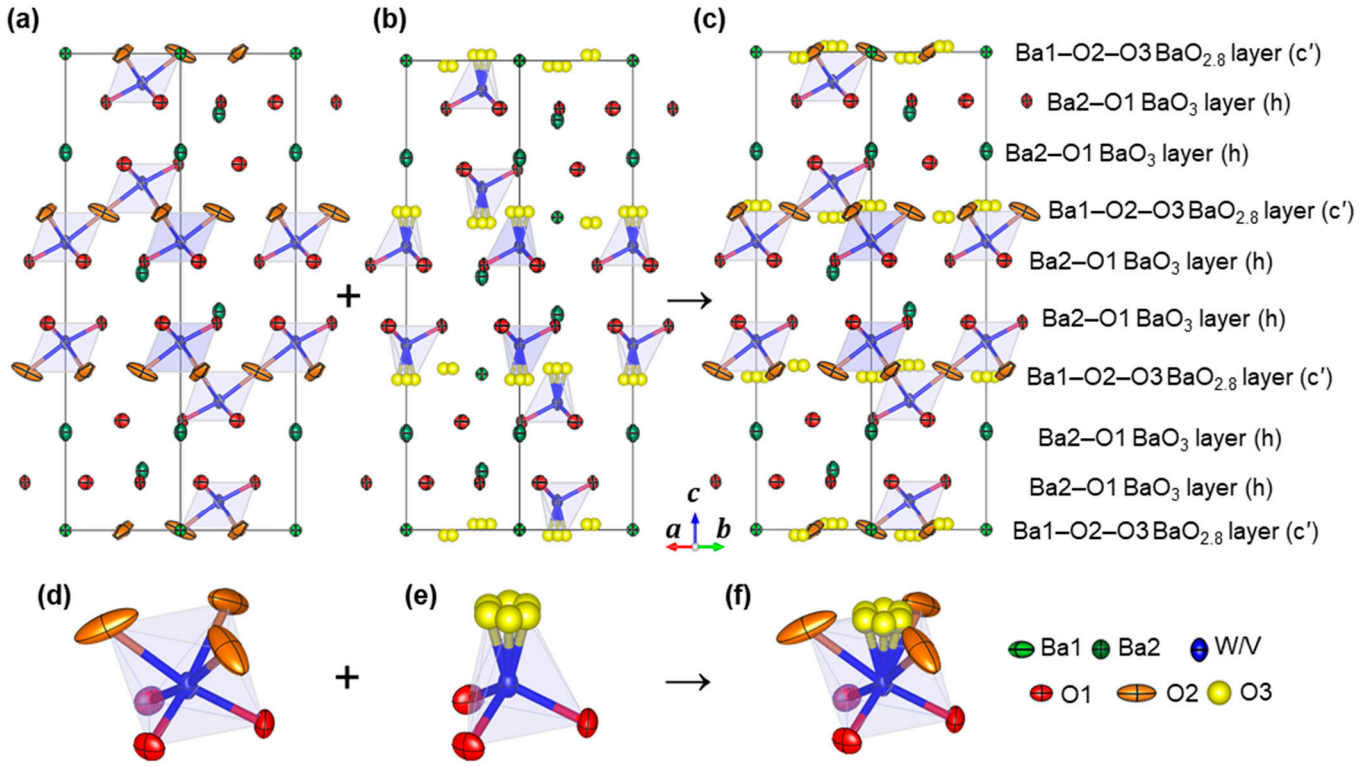

Figure 4. (**c**) Refined crystal structure and (**f**) $(W/V)O_{5.408(7)}$ polyhedron of $Ba_3W_{1.6}V_{0.4}O_{8.8}$, which was obtained using Rietveld analysis and neutron diffraction data taken at 800 °C. The $(W/V)O_{5.408(7)}$ polyhedron in $Ba_3W_{1.6}V_{0.4}O_{8.8}$ (**c**,**f**) is regarded as a hybrid of (**a**,**d**) a $(W/V)O_6$ octahedron and (**b**,**e**) a $(W/V)O_4$ tetrahedron.

Figure 4c shows the crystal structure refined using Rietveld analysis and neutron diffraction data of $Ba_3W_{1.6}V_{0.4}O_{8.8}$ taken at 800 °C. The structure has hexagonal close-packed (h) BaO_3 layers (Ba2–O1 layers) and oxygen-deficient, cubic close-packed (c′) $BaO_{2.8}$ layers (Ba1–O2–O3 layers), forming a sequence of $(hhc')_3$. The $(W/V)O_{5.408(7)}$ polyhedron (Figure 4f) can be regarded as a hybrid of a $(W/V)O_6$ octahedron (Figure 4d) and a $(W/V)O_4$ tetrahedron (Figure 4e). Thus, the crystal structure of $Ba_3W_{1.6}V_{0.4}O_{8.8}$ (Figure 4c) is a hybrid of the structures of Figure 4a,b. The high oxide ion conductivity of $Ba_3W_{1.6}V_{0.4}O_{8.8}$ can be ascribed to the interexchange between the $(W/V)O_4$ tetrahedron and $(W/V)O_6$ octahedron, as discussed below.

2.4. Neutron Scattering Length Density Analyses of $Ba_3W_{1.6}V_{0.4}O_{8.8}$ and $Ba_3WVO_{8.5}$

To discuss the origin of the high oxide ion conductivity of $Ba_3W_{1.6}V_{0.4}O_{8.8}$, neutron scattering length densities (NSLDs) were analyzed via the maximum entropy method (MEM), using the structure factors estimated in the Rietveld analyses of the neutron diffraction data of $Ba_3W_{1.6}V_{0.4}O_{8.8}$ and $Ba_3WVO_{8.5}$ taken in situ at 18 and 800 °C. It is known that MEM enables the visualization of the oxide ion diffusion pathways and structural disorder [18,19,22,27,29]. Figure 5 shows the NSLD distributions and corresponding refined structures of $Ba_3W_{1.6}V_{0.4}O_{8.8}$ at 800 °C. Connected NSLD distributions are clearly observed between the octahedral O2 and tetrahedral O3 atoms, which corresponds to the experimental visualization of the oxide ion O2–O3 diffusion pathways. Figure 5b–d show the two-dimensional network of the O2–O3 diffusion pathways. The oxide ion migrates along the O2–O3 edges of the $(W/V)O_{5.408(7)}$ polyhedron (Figure 4f). These features are similar to other $Ba_3M_2O_{8.5}$ oxides (M_2 = MoNb [19], WNb [27], and WV (this work, Figure 6a,c and [22])).

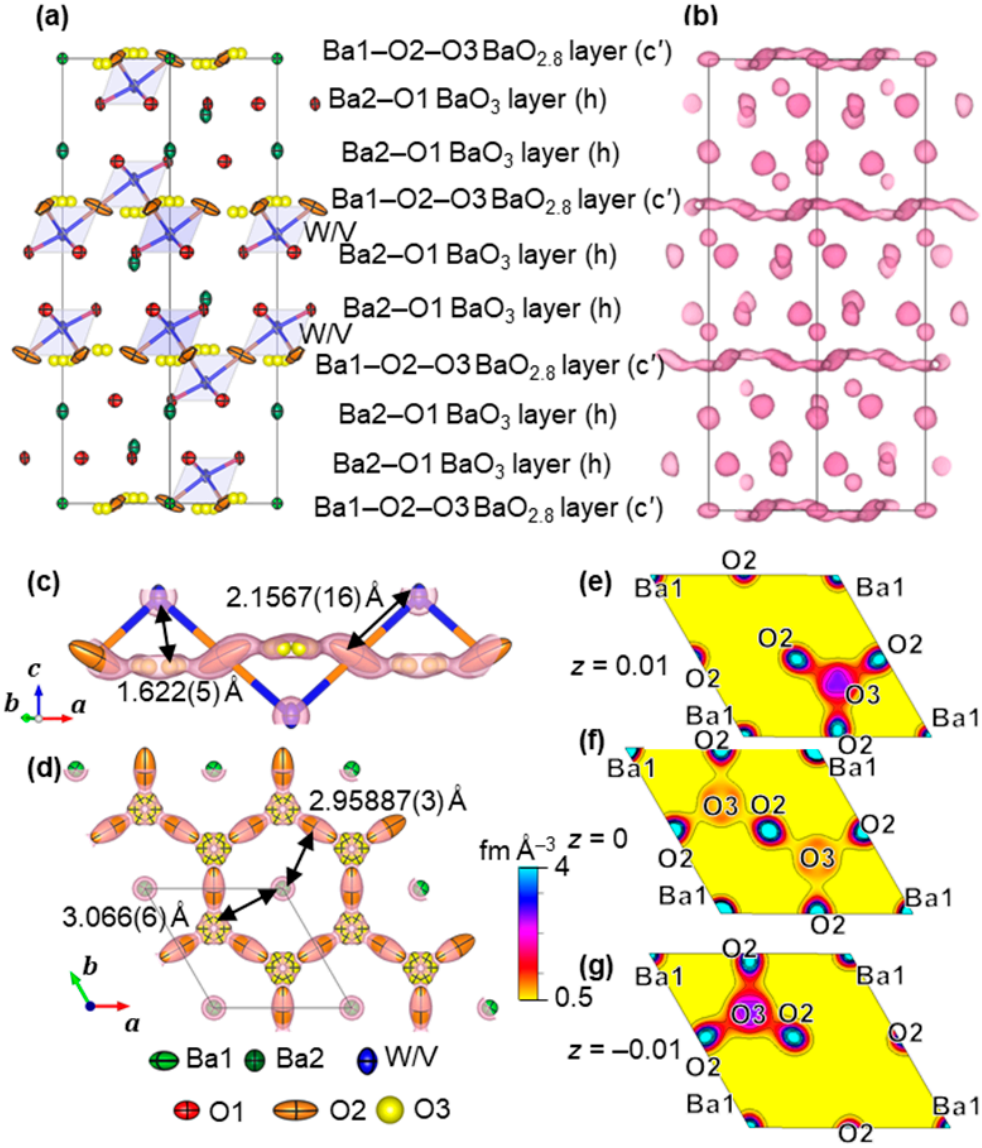

Figure 5. (**a**,**c**,**d**) Refined crystal structure and (**b**–**d**) corresponding isosurface of the neutron scattering length density (NSLD) at 1.0 fm Å^{-3} of $Ba_3W_{1.6}V_{0.4}O_{8.8}$ at 800 °C. NSLD distributions on the *ab* planes at (**e**) $z = 0.01$, (**f**) $z = 0$, and (**g**) $z = -0.01$ of $Ba_3W_{1.6}V_{0.4}O_{8.8}$ at 800 °C. Atomic displacement ellipsoids are drawn at an 80% probability level.

The NSLD distributions around the O2 and O3 sites are localized at 18 °C (Figure 6a,b), while they are connected between the O2 and O3 sites at 800 °C (Figure 6c,d), which is consistent with the higher conductivity at higher temperature (Figures 1a and 2d). The minimum NSLD between the O2 and O3 sites (Figure 6e,f) can be a measure of oxide ion conductivity [27,29]. The minimum NSLD of $Ba_3WVO_{8.5}$ at 800 °C (0.73 fm Å^{-3}) is higher than that at 18 °C (0.08 fm Å^{-3}), which is consistent with the higher conductivity observed at 800 °C (Figures 1a and 2d). Similarly, the minimum NSLD of $Ba_3W_{1.6}V_{0.4}O_{8.8}$ at 800 °C (1.62 fm Å^{-3}) is higher than that at 18 °C (0.95 fm Å^{-3}), which is also consistent with the higher conductivity observed at 800 °C. We have demonstrated that $Ba_3W_{1.6}V_{0.4}O_{8.8}$ exhibits higher oxide ion conductivity compared with the mother material $Ba_3WVO_{8.5}$. The minimum NSLD of $Ba_3W_{1.6}V_{0.4}O_{8.8}$ at 800 °C (1.62 fm Å^{-3}) is higher than that of $Ba_3WVO_{8.5}$ at 800 °C (0.73 fm Å^{-3}), which is consistent with the higher conductivity of $Ba_3W_{1.6}V_{0.4}O_{8.8}$.

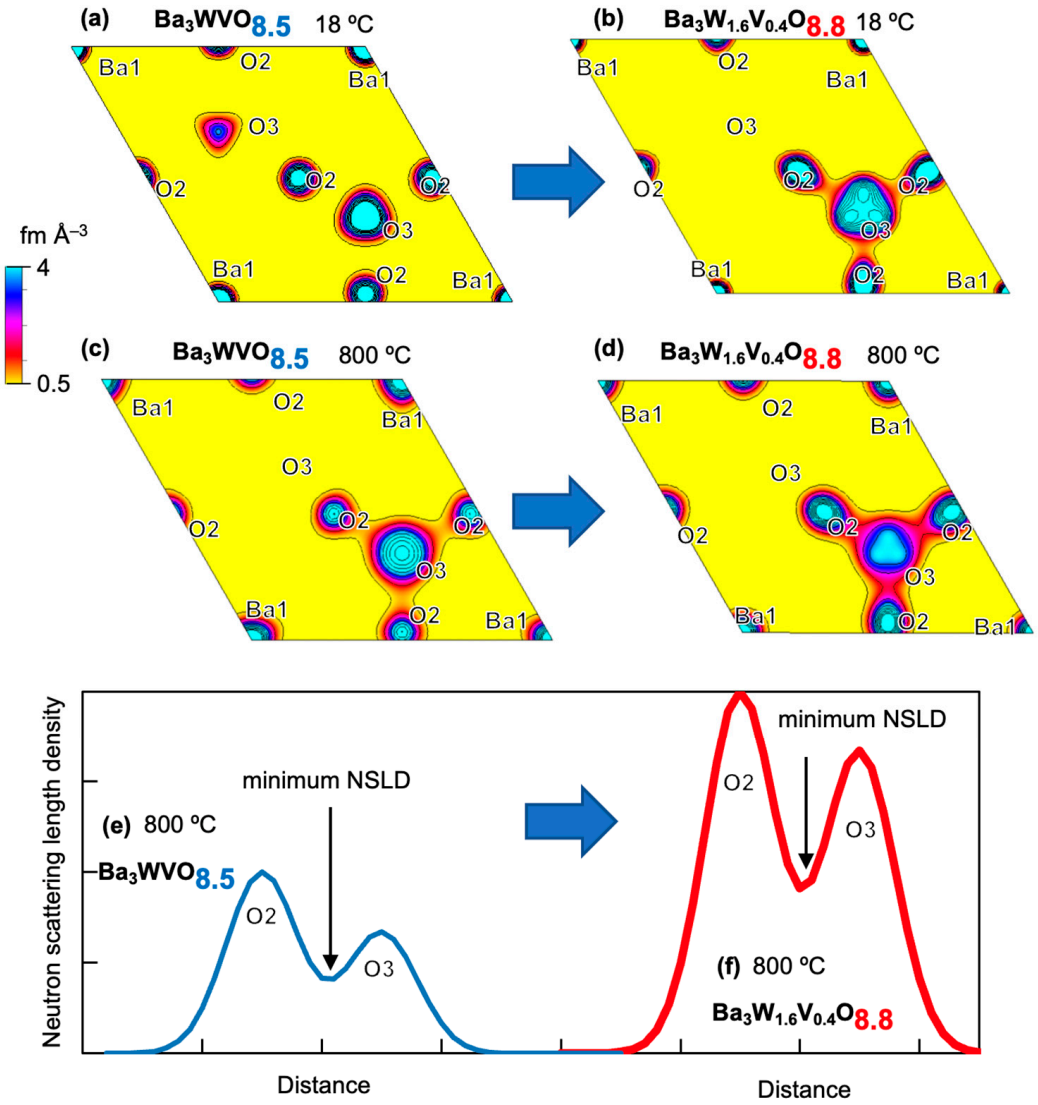

Figure 6. Increased minimum neutron scattering length density (NSLD) between the O2 and O3 sites produced by excess oxygen ($O_{0.3}$), which enhances the oxide ion conductivity. NSLD distributions on the *ab* plane at z = 0.01 of $Ba_3WVO_{8.5}$ (**a**,**c**) and $Ba_3W_{1.6}V_{0.4}O_{8.8}$ (**b**,**d**) at 18 °C (**a**,**b**) and 800 °C (**c**,**d**). Contour lines in the range of 0.5 to 9.5 fm Å^{-3} and 1 fm Å^{-3} per step. Schematic NSLD distributions between the nearest-neighbor O2 and O3 atoms of $Ba_3WVO_{8.5}$ (**e**) and $Ba_3W_{1.6}V_{0.4}O_{8.8}$ (**f**) at 800 °C.

2.5. Structural Origins of High Oxide Ion Conductivity in $Ba_3W_{1.6}V_{0.4}O_{8.8}$

Next, we discuss the origins of the higher conductivity of $Ba_3W_{1.6}V_{0.4}O_{8.8}$ compared with $Ba_3WVO_{8.5}$, based on their NSLD distributions at 800 °C (Figure 6). Figure 6e,f shows schematic NSLD distributions between the nearest-neighbor O2 and O3 sites of $Ba_3WVO_{8.5}$ (e) and $Ba_3W_{1.6}V_{0.4}O_{8.8}$ (f) at 800 °C. $Ba_3W_{1.6}V_{0.4}O_{8.8}$ has 0.3 excess oxygen atoms compared with the mother material $Ba_3WVO_{8.5}$. The excess oxygen atoms are incorporated at the O2 and O3 sites; therefore, the occupancy factors of the O2 and O3 atoms and oxygen content on the c′ layer of $Ba_3W_{1.6}V_{0.4}O_{8.8}$ are higher than those of $Ba_3WVO_{8.5}$. Thus, the NSLD and minimum NSLD between the O2 and O3 sites of $Ba_3W_{1.6}V_{0.4}O_{8.8}$ (e.g., 1.62 fm Å^{-3} at 800 °C) are higher than those of $Ba_3WVO_{8.5}$ (e.g., 0.73 fm Å^{-3} at 800 °C), leading to the higher oxide ion conductivity of $Ba_3W_{1.6}V_{0.4}O_{8.8}$. It is known that O2/O3 occupational disordering can enhance the oxide ion conductivity in $Ba_3WNbO_{8.5}$ [27]. The disorder parameter *DP* was calculated using the formulation of Yasui et al. [27] and the refined crystal parameters in Tables S1–S4. The *DP* of $Ba_3W_{1.6}V_{0.4}O_{8.8}$ (0.7660(15) at 800 °C) is slightly lower than the *DP* of $Ba_3WVO_{8.5}$ (0.860(4) at 800 °C), which cannot

explain the conductivity enhancement observed in $Ba_3W_{1.6}V_{0.4}O_{8.8}$. These results indicate the enhancement of the oxide ion conductivity of $Ba_3W_{1.6}V_{0.4}O_{8.8}$ due to the excess oxygen.

We have indicated that the activation energy for the bulk conductivity of $Ba_3W_{1.6}V_{0.4}O_{8.8}$ (0.741(12) eV) is lower than that of the mother material $Ba_3WVO_{8.5}$ (1.13(1) eV) (Figure 2d). The occupancy factor of the larger W^{6+} cation at the W/V site in $Ba_3W_{1.6}V_{0.4}O_{8.8}$ (0.8) is higher than that in $Ba_3WVO_{8.5}$ (0.5). Therefore, the (W/V)–O2 bond length of $Ba_3W_{1.6}V_{0.4}O_{8.8}$ (2.1567(16) Å at 800 °C) is longer than that of $Ba_3WVO_{8.5}$ (2.123(4) Å at 800 °C). Similarly, the (W/V)–O3 bond length of $Ba_3W_{1.6}V_{0.4}O_{8.8}$ (1.622(5) Å at 800 °C) is longer than that of $Ba_3WVO_{8.5}$ (1.466(8) Å at 800 °C). These results suggest a size effect of the W/V cation on the activation energy for oxide ion conductivity E_a in which the lower E_a of $Ba_3W_{1.6}V_{0.4}O_{8.8}$ can be ascribed to the longer (W/V)–O2 and (W/V)–O3 distances.

3. Materials and Methods

3.1. Synthesis and Characterization of $Ba_3W_{1+x}V_{1-x}O_{8.5+x/2}$ ($x = -0.1, -0.05, 0, 0.05, 0.1, 0.25, 0.4, 0.5, 0.6$, and 0.75)

$Ba_3W_{1+x}V_{1-x}O_{8.5+x/2}$ ($x = -0.1, -0.05, 0, 0.05, 0.1, 0.25, 0.4, 0.5, 0.6, 0.75$) samples were synthesized via high-temperature solid-state reactions. Stoichiometric amounts of $BaCO_3$ (99.9%), WO_3 (99.9%), and V_2O_5 (99.75%) were mixed as ethanol slurries and dry powders using an agate mortar for 1 h. The mixtures were calcined at 950 °C for 15 h in static air. The calcined samples were crushed into powders and mixed again as ethanol slurries and dry powders using the agate mortar for 1 h, followed by ball milling processes using 5, 3, and 1 mm diameter zirconia balls at 300 rpm for 30 min at each size with a FRITSCH PULVERISETTE 7. The powders thus obtained were isostatically pressed into pellets at 150 MPa and sintered at 950–1020 °C for 20 h. The phase purity of $Ba_3W_{1+x}V_{1-x}O_{8.5+x/2}$ were evaluated by XRD measurements using an X-ray diffractometer (Bruker D8, Cu $K\alpha$). The lattice parameters of $Ba_3W_{1+x}V_{1-x}O_{8.5+x/2}$ were refined via the Le Bail analyses of the XRD data of the mixture of $Ba_3W_{1+x}V_{1-x}O_{8.5+x/2}$ and an internal silicon standard using the software FullProf [30].

The chemical composition of $Ba_3W_{1.6}V_{0.4}O_{8.8}$ was examined via energy dispersive XRF (Rigaku, Tokyo, Japan, NEX DE) and ICP-OES (Agilent Technologies, Tokyo, Japan, 5100 VDV) analyses, which validated the nominal composition. The UV-vis diffuse reflectance spectra of $Ba_3W_{1.6}V_{0.4}O_{8.8}$ were measured using JASCO (Tokyo, Japan) V-650 at RT with spectral range of 850–200 nm. The optical band gaps for direct and indirect transitions of $Ba_3W_{1.6}V_{0.4}O_{8.8}$ and $Ba_3WVO_{8.5}$ were estimated using the Kubelka–Munk function and Tauc plots. The weight changes in $Ba_3W_{1.6}V_{0.4}O_{8.8}$ and $Ba_3WVO_{8.5}$ were investigated using an NETZSCH (Yokohama, Japan) STA 449 F3 Jupiter. The temperature range of the measurement was 35–900 °C, with a 2 °C min^{-1} temperature ramp under 50 mL min^{-1} of dry air flow. The XPS spectra of $Ba_3W_{1.6}V_{0.4}O_{8.8}$ and $Ba_3WVO_{8.5}$ were measured using a JPS–9010 X-ray photoelectron spectrometer (JEOL, Tokyo, Japan).

3.2. Electrical Properties of $Ba_3W_{1.6}V_{0.4}O_{8.8}$

The total DC electrical conductivities σ_{DC} of the sintered $Ba_3W_{1+x}V_{1-x}O_{8.5+x/2}$ ($x = -0.1, -0.05, 0, 0.05, 0.1, 0.25, 0.4, 0.5, 0.6$, and 0.75) were measured via a DC four-probe method in static air at 600–1000 °C. Pt electrodes with Pt wires were attached to each pellet. The σ_{DC} of $Ba_3W_{1.6}V_{0.4}O_{8.8}$ was measured in dry and wet (water vapor pressure: $P(H_2O) = 0.023$ atm) air. The $P(O_2)$ dependence of $Ba_3W_{1.6}V_{0.4}O_{8.8}$ was measured at 820 °C in a $P(O_2)$ between 0.21 and 5.4×10^{-25} atm, and the $P(O_2)$ was controlled using a mixture of O_2, N_2, and 5% H_2/N_2 gases and monitored by a YSZ oxygen sensor downstream of the apparatus. The impedance spectra of the sintered $Ba_3W_{1.6}V_{0.4}O_{8.8}$ pellet with Pt electrodes were measured using a Solartron 1260 impedance analyzer in the frequency range of 1 MHz to 100 mHz with an AC voltage of 100 mV. The AC impedance measurements were carried out under a dry air flow from 794 to 382 °C. An equivalent circuit analysis was performed using ZView software (Scribner Associates, Inc., Southern Pines, USA) to exact the bulk and grain boundary conductivities.

3.3. Structural and MEM Neutron Scattering Length Density Analyses Using Neutron Diffraction Data of $Ba_3WVO_{8.5}$ and $Ba_3W_{1.6}V_{0.4}O_{8.8}$

Neutron powder diffraction (ND) patterns of $Ba_3WVO_{8.5}$ and $Ba_3W_{1.6}V_{0.4}O_{8.8}$ were obtained using a fixed-wavelength neutron diffractometer, Echidna [31], at the OPAL research reactor, ANSTO, Australia. The range of 2θ was $10° \leq 2\theta \leq 160°$ at 18 and 800 °C. The ND data were analyzed via the Rietveld method using Z-Rietveld [32,33]. The neutron scattering length density distributions were investigated using the maximum entropy method (MEM). The MEM analyses were performed with the structure factors obtained from the Rietveld analyses of $Ba_3WVO_{8.5}$ and $Ba_3W_{1.6}V_{0.4}O_{8.8}$ using Z-Rietveld [32,33]. The refined crystal structures and NSLD distributions were visualized using VESTA [34].

4. Conclusions

We have synthesized new hexagonal perovskite-related materials: $Ba_3W_{1+x}V_{1-x}O_{8.5+x/2}$ ($x = -0.1$, -0.05, 0.05, 0.1, 0.25, 0.4, 0.5, 0.6, and 0.75). It was found that $Ba_3W_{1.6}V_{0.4}O_{8.8}$ exhibits the highest DC electrical conductivity in static air among the $Ba_3W_{1+x}V_{1-x}O_{8.5+x/2}$ ($-0.1 \leq x \leq 0.75$, Figure 1). Electrical properties and a wide optical band gap indicated the oxide ion conduction of $Ba_3W_{1.6}V_{0.4}O_{8.8}$ (Figures 2 and S4). The bulk conductivity σ_b of $Ba_3W_{1.6}V_{0.4}O_{8.8}$ is higher than that of the mother material $Ba_3WVO_{8.5}$ over the entire temperature range (Figure 2d). The refined crystal structure and MEM NSLD distributions of $Ba_3W_{1.6}V_{0.4}O_{8.8}$ and $Ba_3WVO_{8.5}$ at 800 °C indicated that the oxide ions migrate via the octahedral O2 and tetrahedral O3 sites (Figures 3–5, Tables S1–S4). The O2–O3 distance is short (e.g., 1.5880(6) Å in $Ba_3W_{1.6}V_{0.4}O_{8.8}$ at 800 °C), which suggests an interexchange between the octahedral and tetrahedral geometries and an interstitialcy cooperative diffusion mechanism of the oxide ions, as in $Ba_7Nb_{3.9}Mo_{1.1}O_{20.05}$ [18].

We have demonstrated that the excess amount of W species at the W/V site considerably improves the oxide ion conductivity. A larger excess of W species x produces a larger excess of oxygen $x/2$ in $Ba_3W_{1+x}V_{1-x}O_{8.5+x/2}$, which leads to more oxygen atoms at the O2 and O3 sites in the oxygen-deficient c′ layer. This creates a higher NSLD between the O2 and O3 sites, leading to the higher oxide ion conductivity (Figure 6). Thus, improvement in the oxide ion conductivity via excess oxygen can be a strategy to search for oxide-ion-conducting hexagonal perovskite-related oxides. Another reason for the higher oxide ion conductivity of $Ba_3W_{1.6}V_{0.4}O_{8.8}$ is the lower activation energy for oxide ion conduction (Figure 2d). We have suggested a size effect of the W/V cation on the activation energy for oxide ion conductivity E_a in which the lower E_a of $Ba_3W_{1.6}V_{0.4}O_{8.8}$ can be ascribed to the longer (W/V)–O2 and (W/V)–O3 distances. Therefore, the substitution of the M cation with a larger one in $Ba_3M_2O_{8.5}$ oxides can be another strategy for improving oxide ion conductivity.

Supplementary Materials: The following supporting information can be downloaded at: https://www.mdpi.com/article/10.3390/inorganics11060238/s1, Figure S1: X-ray powder diffraction pattern of $Ba_3W_{1.6}V_{0.4}O_8$, lattice parameters and lattice volume of $Ba_3W_{1+x}V_{1-x}O_{8.5+x/2}$ as functions of excess W content x; Figure S2: XPS spectra of $Ba_3W_{1.6}V_{0.4}O_{8.8}$ and $Ba_3WVO_{8.5}$; Figure S3: Thermogravimetric curves of $Ba_3W_{1.6}V_{0.4}O_{8.8}$; Figure S4: Diffuse reflectance spectra and Tauc plots of $Ba_3W_{1.6}V_{0.4}O_{8.8}$; Figure S5: Equivalent circuits and complex impedance plots of $Ba_3W_{1.6}V_{0.4}O_{8.8}$; Figure S6: Arrhenius plots of bulk and grain boundary conductivities of $Ba_3W_{1.6}V_{0.4}O_{8.8}$; Table S1: Refined crystallographic parameters and reliability factors of the neutron diffraction data of $Ba_3W_{1.6}V_{0.4}O_{8.8}$ at 18 °C; Table S2: Refined crystallographic parameters and reliability factors of the neutron diffraction data of $Ba_3WVO_{8.5}$ at 18 °C; Table S3: Refined crystallographic parameters and reliability factors of the neutron diffraction data of $Ba_3W_{1.6}V_{0.4}O_{8.8}$ at 800 °C; Table S4: Refined crystallographic parameters and reliability factors of the neutron diffraction data of $Ba_3WVO_{8.5}$ at 800 °C; Supplementary Note: Influence of $BaWO_4$ impurity on the electrical conductivity of $Ba_3W_{1.6}V_{0.4}O_{8.8}$. References [35–39] are cited in the supplementary materials.

Author Contributions: Y.K. and M.Y. conceived and designed the experiments; Y.K. and Y.Y. performed the conductivity measurements; J.R.H. performed the neutron diffraction experiments; Y.K. and Y.Y. analyzed the neutron data; Y.K., Y.Y. and M.Y. wrote the original draft of the manuscript; M.Y. edited and revised the manuscript; M.Y. provided supervision, project administration, and funding acquisition. All authors have read and agreed to the published version of the manuscript.

Funding: This research was funded by Grants-in-Aid for Scientific Research (KAKENHI, JP19H00821, JP21K18182) from the Ministry of Education, Culture, Sports, Science and Technology of Japan, Adaptable and Seamless Technology Transfer Program through Target-driven R&D (A-STEP) from the Japan Science and Technology Agency (JST), Grant Number JPMJTR22TC, and JSPS Core-to-Core Programs, A. Advanced Research Networks, Grant number: JPJSCCA20200004. Y.Y. acknowledges support in the form of a JSPS Fellowship for Young Scientists, DC1 (JP20J23124). The travel costs were partially supported by the Institute for Solid State Physics, The University of Tokyo (proposal No. 15616, 16604, and 16595).

Data Availability Statement: The data that support the findings of this study are available from the corresponding author, [M.Y.], upon reasonable request.

Acknowledgments: We express special thanks to T. Murakami, K. Fujii, W. Zhang, and H. Yaguchi for useful discussion and assistance in the experiments/analyses. We thank S. Iguchi for the assistance in the XPS measurements. Neutron diffraction measurements were carried out by the project approval (ANSTO: Proposal Nos. PPR6342, PP5198, and PPR5618; J-PARC: Proposal No. 2020L801, 2017L1300, 2017L1301 and 2017L1302). Synchrotron X-ray diffraction experiments were performed by the project approval (PF: 2014G508, 2015G047, 2016G644, 2017G168, and 2018G543; SPring-8: 2019A1052 and 2021A1599).

Conflicts of Interest: The authors declare no conflict of interest.

References

1. Nakayama, S.; Kageyama, T.; Aono, H.; Sadaoka, Y. Ionic Conductivity of Lanthanoid Silicates, $Ln_{10}(SiO_4)_6O_3$ (*Ln*=La, Nd, Sm, Gd, Dy, Y, Ho, Er and Yb). *J. Mater. Chem.* **1995**, *5*, 1801–1805. [CrossRef]
2. Brett, D.J.L.; Atkinson, A.; Brandon, N.P.; Skinner, S.J. Intermediate Temperature Solid Oxide Fuel Cells. *Chem. Soc. Rev.* **2008**, *37*, 1568–1578. [CrossRef] [PubMed]
3. Li, X.; Zhao, H.; Liang, J.; Luo, Y.; Chen, G.; Shi, X.; Lu, S.; Gao, S.; Hu, J.; Liu, Q.; et al. A-site perovskite oxides: An emerging functional material for electrocatalysis and photocatalysis. *J. Mater. Chem. A* **2021**, *9*, 6650–6670. [CrossRef]
4. Jacobson, A.J. Materials for Solid Oxide Fuel Cells. *Chem. Mater.* **2010**, *22*, 660–674. [CrossRef]
5. Liao, Y.W.; Kawabata, S.; Yabutsuka, T.; Chen, W.J.; Okumura, H.; Takai, S. Low Temperature Phase Transition Phenomena in Ba- and Pb-Substituted $La_2Mo_2O_9$ Oxide Ion Conductors. *Solid State Ionics* **2020**, *354*, 115405. [CrossRef]
6. Kharton, V.V.; Tsipis, E.V.; Kolotygin, V.A.; Avdeev, M.; Kennedy, B.J. Ionic Conductivity and Thermal Expansion of Anion-Deficient $Sr_{11}Mo_4O_{23}$ Perovskite. *J. Solid State Electrochem.* **2020**, *24*, 2943–2951. [CrossRef]
7. Gazda, M.; Miruszewski, T.; Jaworski, D.; Mielewczyk-Gryń, A.; Skubida, W.; Wachowski, S.; Winiarz, P.; Dzierzgowski, K.; Łapiński, M.; Szpunar, I.; et al. Novel Class of Proton Conducting Materials—High Entropy Oxides. *ACS Mater. Lett.* **2020**, *2*, 1315–1321. [CrossRef]
8. Istomin, S.Y.; Lyskov, N.V.; Mazo, G.N.; Antipov, E.V. Electrode Materials Based on Complex D-Metal Oxides for Symmetrical Solid Oxide Fuel Cells. *Russ. Chem. Rev.* **2021**, *90*, 644–676. [CrossRef]
9. Tarasova, N.A.; Animitsa, I.E.; Galisheva, A.O.; Medvedev, D.A. Layered and Hexagonal Perovskites as Novel Classes of Proton-Conducting Solid Electrolytes. A Focus Review. *Electrochem. Mater. Technol.* **2022**, *1*, 20221004. [CrossRef]
10. Coduri, M.; Karlsson, M.; Malavasi, L. Structure–Property Correlation in Oxide-Ion and Proton Conductors for Clean Energy Applications: Recent Experimental and Computational Advancements. *J. Mater. Chem. A* **2022**, *10*, 5082–5110. [CrossRef]
11. Zhang, W.; Yashima, M. Recent Developments in Oxide Ion Conductors: Focusing on Dion–Jacobson Phases. *Chem. Commun.* **2023**, *59*, 134–152. [CrossRef] [PubMed]
12. Yasui, Y.; Tansho, M.; Fujii, K.; Sakuda, Y.; Goto, A.; Ohki, S.; Mogami, Y.; Iijima, T.; Kobayashi, S.; Kawaguchi, S.; et al. Hidden Chemical Order in Disordered $Ba_7Nb_4MoO_{20}$ Revealed by Resonant X-Ray Diffraction and Solid-State NMR. *Nat. Commun.* **2023**, *14*, 2337. [CrossRef] [PubMed]
13. Andreev, R.D.; Korona, D.V.; Anokhina, I.A.; Animitsa, I.E. Novel Nb^{5+}-doped hexagonal perovskite $Ba_5In_2Al_2ZrO_{13}$ (structure, hydration, electrical conductivity). *Chim. Techno Acta* **2022**, *9*, 20229414. [CrossRef]
14. Kluczny, M.; Song, J.T.; Akbay, T.; Niwa, E.; Takagaki, A.; Ishihara, T. Sillén–Aurivillius Phase Bismuth Niobium Oxychloride, Bi_4NbO_8Cl, as a New Oxide-Ion Conductor. *J. Mater. Chem. A* **2022**, *10*, 2550–2558. [CrossRef]
15. Huang, K.; Feng, M.; Goodenough, J.B. Synthesis and Electrical Properties of Dense $Ce_{0.9}Gd_{0.1}O_{1.95}$ Ceramics. *J. Am. Ceram. Soc.* **2005**, *81*, 357–362. [CrossRef]

16. Ishihara, T.; Matsuda, H.; Takita, Y. Doped $LaGaO_3$ Perovskite Type Oxide as a New Oxide Ionic Conductor. *J. Am. Chem. Soc.* **1994**, *116*, 3801–3803. [CrossRef]
17. Kwon, O.H.; Choi, G.M. Electrical Conductivity of Thick Film YSZ. *Solid State Ionics* **2006**, *177*, 3057–3062. [CrossRef]
18. Yashima, M.; Tsujiguchi, T.; Sakuda, Y.; Yasui, Y.; Zhou, Y.; Fujii, K.; Torii, S.; Kamiyama, T.; Skinner, S.J. High Oxide-Ion Conductivity through the Interstitial Oxygen Site in $Ba_7Nb_4MoO_{20}$-Based Hexagonal Perovskite Related Oxides. *Nat. Commun.* **2021**, *12*, 556. [CrossRef]
19. Yashima, M.; Tsujiguchi, T.; Fujii, K.; Niwa, E.; Nishioka, S.; Hester, J.R.; Maeda, K. Direct Evidence for Two-Dimensional Oxide-Ion Diffusion in the Hexagonal Perovskite-Related Oxide $Ba_3MoNbO_{8.5-\delta}$. *J. Mater. Chem. A* **2019**, *7*, 13910–13916. [CrossRef]
20. McCombie, K.S.; Wildman, E.J.; Ritter, C.; Smith, R.I.; Skakle, J.M.S.; Mclaughlin, A.C. Relationship between the Crystal Structure and Electrical Properties of Oxide Ion Conducting $Ba_3W_{1.2}Nb_{0.8}O_{8.6}$. *Inorg. Chem.* **2018**, *57*, 11942–11947. [CrossRef]
21. Gilane, A.; Fop, S.; Sher, F.; Smith, R.I.; Mclaughlin, A.C. The Relationship between Oxide-Ion Conductivity and Cation Vacancy Order in the Hybrid Hexagonal Perovskite $Ba_3VWO_{8.5}$. *J. Mater. Chem. A* **2020**, *8*, 16506–16514. [CrossRef]
22. Gilane, A.; Fop, S.; Tawse, D.N.; Ritter, C.; Mclaughlin, A.C. Variable Temperature Neutron Diffraction Study of the Oxide Ion Conductor $Ba_3VWO_{8.5}$. *Inorg. Chem.* **2022**, *61*, 1597–1602. [CrossRef] [PubMed]
23. Kuang, X.; Allix, M.; Ibberson, R.M.; Claridge, J.B.; Niu, H.; Rosseinsky, M.J. Oxygen Vacancy Ordering Phenomena in the Mixed-Conducting Hexagonal Perovskite $Ba_7Y_2Mn_3Ti_2O_{20}$. *Chem. Mater.* **2007**, *19*, 2884–2893. [CrossRef]
24. Fop, S.; Skakle, J.M.S.; McLaughlin, A.C.; Connor, P.A.; Irvine, J.T.S.; Smith, R.I.; Wildman, E.J. Oxide Ion Conductivity in the Hexagonal Perovskite Derivative $Ba_3MoNbO_{8.5}$. *J. Am. Chem. Soc.* **2016**, *138*, 16764–16769. [CrossRef]
25. Bernasconi, A.; Tealdi, C.; Malavasi, L. High-Temperature Structural Evolution in the $Ba_3Mo_{(1-x)}W_xNbO_{8.5}$ System and Correlation with Ionic Transport Properties. *Inorg. Chem.* **2018**, *57*, 6746–6752. [CrossRef]
26. Murakami, T.; Shibata, T.; Yasui, Y.; Fujii, K.; Hester, J.R.; Yashima, M. High Oxide-Ion Conductivity in a Hexagonal Perovskite-Related Oxide $Ba_7Ta_{3.7}Mo_{1.3}O_{20.15}$ with Cation Site Preference and Interstitial Oxide Ions. *Small* **2022**, *18*, 2106785. [CrossRef]
27. Yasui, Y.; Tsujiguchi, T.; Sakuda, Y.; Hester, J.R.; Yashima, M. Oxide-Ion Occupational Disorder, Diffusion Path, and Conductivity in Hexagonal Perovskite Derivatives $Ba_3WNbO_{8.5}$ and $Ba_3MoNbO_{8.5}$. *J. Phys. Chem. C* **2022**, *126*, 2383–2393. [CrossRef]
28. El Khal, H.; Cordier, A.; Batis, N.; Siebert, E.; Georges, S.; Steil, M.C. Effect of Porosity on the Electrical Conductivity of LAMOX Materials. *Solid State Ionics* **2017**, *304*, 75–84. [CrossRef]
29. Yashima, M.; Yamada, H.; Nuansaeng, S.; Ishihara, T. Role of Ga^{3+} and Cu^{2+} in the High Interstitial Oxide-Ion Diffusivity of Pr_2NiO_4-Based Oxides: Design Concept of Interstitial Ion Conductors through the Higher-Valence d^{10} Dopant and Jahn–Teller Effect. *Chem. Mater.* **2012**, *24*, 4100–4113. [CrossRef]
30. Rodriguez-Carvajal, J. Nouveaux Développements de FullProf Analyse de La Microstructure et Utilisation Du Recuit Simulé Pour La Résolution de Structures. *Comm. Powder Diffr. (IUCr) Newsl.* **2001**, *26*, 12–19.
31. Avdeev, M.; Hester, J.R. ECHIDNA: A Decade of High-Resolution Neutron Powder Diffraction at OPAL. *J. Appl. Crystallogr.* **2018**, *51*, 1597–1604. [CrossRef]
32. Oishi, R.; Yonemura, M.; Nishimaki, Y.; Torii, S.; Hoshikawa, A.; Ishigaki, T.; Morishima, T.; Mori, K.; Kamiyama, T. Rietveld Analysis Software for J-PARC. *Nucl. Instrum. Methods Phys. Res. Sect. A Accel. Spectrometers Detect. Assoc. Equip.* **2009**, *600*, 94–96. [CrossRef]
33. Oishi-Tomiyasu, R.; Yonemura, M.; Morishima, T.; Hoshikawa, A.; Torii, S.; Ishigaki, T.; Kamiyama, T. Application of Matrix Decomposition Algorithms for Singular Matrices to the Pawley Method in Z-Rietveld. *J. Appl. Crystallogr.* **2012**, *45*, 299–308. [CrossRef]
34. Momma, K.; Izumi, F. *VESTA 3* for Three-Dimensional Visualization of Crystal, Volumetric and Morphology Data. *J. Appl. Crystallogr.* **2011**, *44*, 1272–1276. [CrossRef]
35. Światowska-Mrowiecka, J.; Maurice, V.; Zanna, S.; Klein, L.; Marcus, P. XPS Study of Li Ion Intercalation in V_2O_5 Thin Films Prepared by Thermal Oxidation of Vanadium Metal. *Electrochim. Acta* **2007**, *52*, 5644–5653. [CrossRef]
36. Fleisch, T.H.; Mains, G.J. An XPS Study of the UV Reduction and Photochromism of MoO_3 and WO_3. *J. Chem. Phys.* **1982**, *76*, 780–786. [CrossRef]
37. Khyzhun, O.Y. XPS, XES and XAS Studies of the Electronic Structure of Tungsten Oxides. *J. Alloys Compd.* **2000**, *305*, 1–6. [CrossRef]
38. Adams, S.; Rao, R.P. High Power Lithium Ion Battery Materials by Computational Design. *Phys. Status Solidi* **2011**, *208*, 1746–1753. [CrossRef]
39. Sahmi, A.; Omeiri, S.; Bensadok, K.; Trari, M. Electrochemical properties of the scheelite $BaWO_4$ prepared by co-precipitation: Application to electro-photocatalysis of ibuprofen degradation. *Mater. Sci. Semicond. Process.* **2019**, *91*, 108–114. [CrossRef]